

Nonreciprocity realized with quantum nonlinearity

Andrés Rosario Hamann,^{1,*} Clemens Müller,^{1,2} Markus Jerger,¹ Maximilian Zanner,³ Joshua Combes,¹ Mikhail Pletyukhov,⁴ Martin Weides,^{3,5} Thomas M. Stace,¹ and Arkady Fedorov^{1,†}

¹ARC Centre of Excellence for Engineered Quantum Systems, School of Mathematics and Physics, The University of Queensland, Saint Lucia, Queensland 4072, Australia

²Institute for Theoretical Physics, ETH Zürich, 8093 Zürich, Switzerland

³Physikalisches Institut, Karlsruhe Institute of Technology (KIT), 76131 Karlsruhe, Germany

⁴Institute for Theory of Statistical Physics, RWTH Aachen University, 52056 Aachen, Germany

⁵School of Engineering, Electronics & Nanoscale Engineering Division, University of Glasgow, Glasgow G12 8QQ, UK

(Dated: September 15, 2022)

Nonreciprocal devices are a key element for signal routing and noise isolation. Rapid development of quantum technologies has boosted the demand for a new generation of miniaturized and low-loss nonreciprocal components. Here we use a pair of tunable superconducting artificial atoms in a 1D waveguide to experimentally realize a minimal passive nonreciprocal device. Taking advantage of the quantum nonlinear behavior of artificial atoms, we achieve nonreciprocal transmission through the waveguide in a wide range of powers. Our results are consistent with theoretical modeling showing that nonreciprocity is associated with the population of the two-qubit nonlocal entangled quasi-dark state, which responds asymmetrically to incident fields from opposing directions. Our experiment highlights the role of quantum correlations in enabling nonreciprocal behavior and opens a path to building passive quantum nonreciprocal devices without magnetic fields.

Microwave nonreciprocal devices based on ferromagnetic compounds increase signal processing capabilities, but they are bulky and inherently lossy [1]. Different approaches to achieve nonreciprocity on a chip are being actively pursued to enable circuits of greater complexity and advanced functionality. A common path to achieve nonreciprocity consists in breaking time-reversal symmetry, either by utilizing novel materials [2–4] or by exploiting sophisticated time control schemes [5–10]. Here we follow another path and use a pair of tunable superconducting artificial atoms in a 1D waveguide in order to realize the simplest possible nonreciprocal device without breaking time-reversal symmetry. In contrast to isolators based on nonlinear bulk media response [11, 12], nonlinear resonances [13], or nonlinearity enhanced by active breaking of the parity-time symmetry [14], our system exploits the quantum nonlinear behavior of a minimal system comprised of two two-level artificial atoms [15–18]. This quantum nonlinearity, combined with an asymmetric atomic detuning that breaks the structural symmetry of the system, leads to population trapping of an entangled state and, ultimately, to 15 dB isolation in a wide range of powers controllable by the experimental settings. Our experiment provides insights into the role of quantum correlations in generating nonreciprocity and open a new path towards the realization of nonreciprocal quantum devices on a chip.

The model of a *quantum diode* built of two atoms in 1D open space was originally proposed in Ref. [15] and has attracted significant theoretical attention since [16–18]. The quantum theory of the diode was first presented in Refs. [9, 16, 17] and later work revealed the

detailed mechanism of nonreciprocity, determining analytical bounds for the device efficiency and identifying entanglement between the atoms and the electromagnetic field as a crucial element in the nonreciprocal behavior of the system [18]. In this work, we present experimental results on the realization of the quantum diode and provide compelling evidence of the connection of its nonreciprocity with the population of the entangled quasi-dark state.

More specifically, we use two transmon-type superconducting qubits inserted in a rectangular copper waveguide (see Fig. 1c). The qubits are spatially separated by $d = 22.5$ mm and are oriented to maximize coupling to the TE_{10} mode, which has a lower cutoff at $f_{c,10} = 6.55$ GHz. Two microwave connectors are positioned near each end of the waveguide, providing an interface between the microwave field inside the waveguide and the external circuitry. This ensures that the qubits are coupled to the continuum of the electromagnetic modes, thus emulating an effective 1D open space. Further technical details into the transmons and 1D waveguide design and characterization can be found in Ref. [19].

The qubits were patterned by standard electron-beam lithographic techniques on high resistivity Si, followed by two angle shadow evaporation of Al. The design of the circuit consists of two planar capacitor plates connected via a line interrupted by a SQUID, playing the role of a tunable Josephson junction (see inset Fig. 1c). The transition frequencies of the qubits are then controlled via two current-biased superconducting coils.

As a result of the interaction with the waveguide modes, the excited state of a qubit $|e\rangle$ spontaneously relaxes to its ground state $|g\rangle$ at the radiative decay rate $\gamma_r/2\pi$. This interaction leads to an almost full reflection of incident resonant microwaves by the qubit at low powers [20], a phenomenon we use to determine the fre-

* arosario@uq.edu.au

† a.fedorov@uq.edu.au

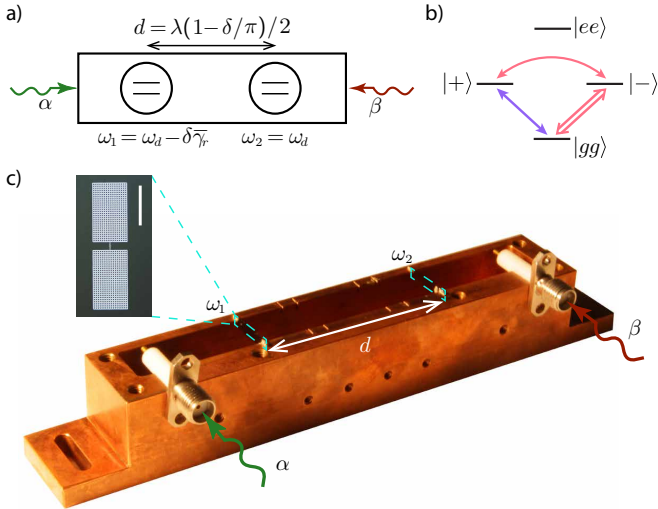


Figure 1. a) Schematic of the quantum diode: two qubits embedded in a 1D waveguide, tuned to the optimal conditions for nonreciprocal behavior ($\omega_1 = \omega_d - \delta\bar{\gamma}_r$, $\omega_2 = \omega_d$). An incoming field from the forward direction (α drive) at frequency ω_d is partially transmitted through the system, whereas a field incoming from the reverse direction (β drive) is fully reflected. b) Energy level diagram of the system. The quasi-dark state $|+\rangle$ can be populated by the driving field either directly from the ground state $|gg\rangle$ (purple path) or indirectly through the bright state $|-\rangle$ (pink path). These two channels interfere either constructively or destructively depending on the driving direction. If interfering constructively, part of the population gets trapped in the quasi-dark state $|+\rangle$, which in turn gives rise to the nonreciprocal behavior of the system. c) Open 1D waveguide with embedded 3D transmons (dashed mint green boxes). Inset: Optical micrograph of one of the two identical 3D transmons. The scale bar corresponds to 500 μm .

quency of our qubits, their radiative decay rates and their decoherence due to other noise channels (refer to the Supplementary Material for more details). The rates $\gamma_r/2\pi$ were found to depend on the transition frequencies of the qubits f_{ge} , and varied between 60 MHz and 85 MHz for f_{ge} between 8.5 GHz and 9.0 GHz, respectively. The transmittance at resonance with the qubit was extinguished to less than 0.4% at low powers of incident radiation, providing an upper bound on the qubits' decoherence rate. This is characterized by the non-radiative decay γ_{nr} and dephasing γ_ϕ rates, which we measured to fall below 0.5% γ_r for both qubits (detailed values can be found in the Supplementary Material). In order to determine the dependence of f_{ge} on the external magnetic field supplied by the coils, we performed transmission measurements while varying the magnetic field produced by each coil. We found the maximum frequencies of the qubits to be 9.9 GHz and 11.0 GHz.

When the two-atom system is driven by an external microwave field, their interaction depends strongly on the distance between qubits. Specifically, the interatomic distance d determines the phase ϕ acquired by the drive when traveling from one qubit to the other, $\phi = \omega_d d / v_p$,

where v_p is the phase velocity in the waveguide and ω_d is the frequency of the drive. We tune ϕ *in situ* by setting the frequency ω_d of the incoming drive.

This interaction between the two qubits with the continuum of the electromagnetic modes in the waveguide gives rise to a field mediated exchange coupling between the qubits described via the term [21] $H_C = \frac{1}{2} \bar{\gamma}_r \sin \phi \left(\sigma_-^{(1)} \sigma_+^{(2)} + \text{h.c.} \right)$, where $\sigma_- = |g\rangle \langle e|$ and $\bar{\gamma}_r \equiv \sqrt{\gamma_{r,1}\gamma_{r,2}}$ (see Supplementary Material). At the phase matching condition $\phi = \pi$ (which, in the case of our system occurs when $\omega_d = \omega_\pi$, with $\omega_\pi \equiv 8.975$ GHz), the exchange coupling between the qubits vanishes, so that the symmetric and antisymmetric states $|\pm\rangle = (|ge\rangle \pm |eg\rangle) / \sqrt{2}$ are perfectly degenerate. Furthermore, the antisymmetric state $|-\rangle$ is bright, with a decay rate $\Gamma_- = 2\bar{\gamma}_r$, whereas the symmetric state $|+\rangle$ is dark, and hence fully decoupled from the interaction with the waveguide modes: $\Gamma_+ = 0$ [21].

If the qubits are slightly detuned from the frequency ω_π , a resonant field at ω_d acquires a phase $\phi = (\omega_d/\omega_\pi)\pi \equiv \pi - \delta$, where the small parameter $\delta \ll 1$ characterizes the detuning from the phase matching condition. In this case, the exchange interaction between qubits does not vanish and lifts in turn the degeneracy between the $|\pm\rangle$ states: $H_C = (J/2)(\sigma_+^{(1)} \sigma_-^{(2)} + \text{h.c.})$, with $J = \bar{\gamma}_r \sin \phi \simeq \bar{\gamma}_r \delta$. To leading order in δ , the dark state $|+\rangle$ becomes quasi-dark with a decay rate $\Gamma_+ = \delta^2 \bar{\gamma}_r$, while the bright state decay rate remains unchanged: $\Gamma_- = 2\bar{\gamma}_r$, [18, 22].

To break the inversion symmetry of our device and achieve nonreciprocal behavior, we set qubit 2 to be resonant with the incoming field, $\omega_2 = \omega_d$, whereas qubit 1 is set at $\omega_1 = \omega_d - \delta\bar{\gamma}_r$, to compensate for the phase asymmetry introduced by the detuned ω_d (see Fig. 1a). This configuration opens an additional path of accessing the quasi-dark state $|+\rangle$, which can now be populated either directly by the incoming field ($|gg\rangle \leftrightarrow |+\rangle$) or indirectly through the bright state ($|gg\rangle \leftrightarrow |-\rangle \leftrightarrow |+\rangle$), to which it is coupled via the exchange term (Fig. 1b).

Our measurement setup allows us to drive the system from either the forward or reverse direction (α and β driving, respectively, in Fig. 1a), with the reflected and transmitted fields simultaneously detected at both sides (refer to the Supplementary Material for extra details on the measurement setup). When driving in the forward direction, both channels to populate the quasi-dark state $|+\rangle$ interfere constructively, giving rise to an excitation of $|+\rangle$. Neglecting non-radiative decay and dephasing ($\gamma_{nr} = \gamma_\phi = 0$), the resulting steady state solution for the density operator of the qubits can be found analytically [18] as $\rho_{st} = (1/3)|gg\rangle\langle gg| + (2/3)|+\rangle\langle +| + O(\delta^2)$ for intermediate driving powers $\delta^2 \bar{\gamma}_r \ll p \ll 2\bar{\gamma}_r$. Under these conditions, the system is predominantly trapped in the quasi-dark state $|+\rangle$ and is therefore partially transparent to the incident signal, due to the extremely low saturability of $|+\rangle$.

If the system is driven in the reverse direction, both

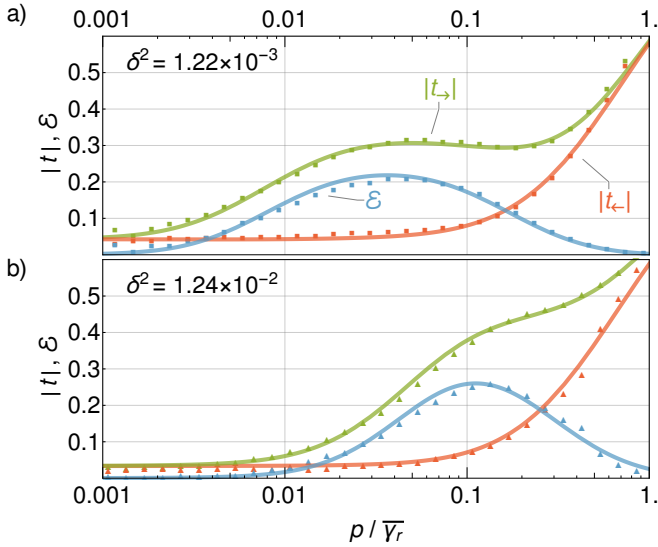


Figure 2. Nonreciprocity dependence on power. Experimental data (points) and theoretical fits (solid lines) for the forward driving transmission amplitude $|t_{\rightarrow}|$ (green), reverse driving transmission amplitude $|t_{\leftarrow}|$ (red) and diode efficiency \mathcal{E} (blue). $\mathcal{E} \equiv |t_{\rightarrow}|(|t_{\rightarrow}| - |t_{\leftarrow}|)/(|t_{\rightarrow}| + |t_{\leftarrow}|)$ measures the nonreciprocal behavior of the system as well as its forward transmitting capabilities. The system is tuned to its optimal nonreciprocal configuration for two different detunings: a) $\delta^2 \simeq 0.001$, b) $\delta^2 \simeq 0.01$. In both cases the device behaves reciprocally and reflects most of the incoming radiation at the low power regime $p/\bar{\gamma}_r \ll \delta^2$. However, as the power increases past the onset of the diode regime, indicated by δ^2 , saturation of the quasi-dark state allows for an increase in $|t_{\rightarrow}|$, while $|t_{\leftarrow}|$ remains unchanged.

channels interfere destructively, the quasi-dark state remains unpopulated and the steady state solution is given by $\rho_{ss} = |gg\rangle\langle gg| + O(\delta^2)$ for powers $p \ll 2\bar{\gamma}_r$. In this case, the incoming signal is reflected by the bright state and the two-qubit system behaves as a mirror.

To illustrate the mechanism of nonreciprocal transmission, we tune the system to its optimal nonreciprocal configuration (up to experimental uncertainties) for two different values of the parameter δ : $\delta^2 \simeq 10^{-2}$ and $\delta^2 \simeq 10^{-3}$, corresponding to driving frequencies $\omega_d \simeq 8.8358$ GHz and $\omega_d \simeq 8.6188$ GHz, respectively.

By controlling the driving power, we are able to probe three characteristic regimes of the device, featured in Fig. 2:

- In the low power regime, $p/\bar{\gamma}_r \ll \delta^2$, the device behaves reciprocally, reflecting most of the incoming radiation. In this regime, the degree of transmission suppression is only limited by the qubits' decoherence and relaxation rates, and by the accuracy of qubit tuning to ensure that $\omega_2 = \omega_d$.
- In the intermediate power regime, $\delta^2 \ll p/\bar{\gamma}_r \ll 1$, the transmission amplitude in the forward direction t_{\rightarrow} increases and features the characteristic plateau

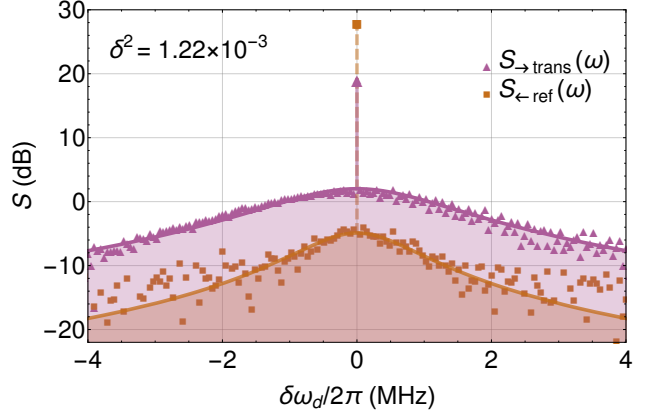


Figure 3. Power spectral densities of the forward driving transmitted field ($S_{\rightarrow\text{trans}}(\omega)$) and the reverse driving reflected field ($S_{\leftarrow\text{ref}}(\omega)$). Both spectra were taken after tuning the device to its optimum nonreciprocal configuration for $\delta^2 \simeq 0.001$ (as in Fig. 2a) and setting the driving power such that the diode efficiency \mathcal{E} is maximum (corresponding to $p/\bar{\gamma}_r \simeq 0.05$ in Fig. 2a). Both scattered fields travel through the same amplification chain. The δ -like peaks at the driving frequency ω_d correspond to the elastically scattered fields. Radiation inelastically scattered off the quasi-dark state $|+\rangle$ generates an additional broader peak, which we fit to Lorentzians of width $\gamma_{\rightarrow\text{trans}} = 2.92$ MHz and $\gamma_{\leftarrow\text{ref}} = 1.76$ MHz (solid lines). When driving the system in the forward direction, part of the population gets trapped in the quasi-dark state, consistent with a greater inelastically scattered radiation power: $\int S_{\rightarrow\text{trans}} d\omega \gg \int S_{\leftarrow\text{ref}} d\omega$.

predicted by theory [16, 18]. The transmission amplitude in the reverse direction t_{\leftarrow} remains near zero independently of the value of $p/\bar{\gamma}_r$ and the system behaves nonreciprocally.

- In the high power regime, $p/\bar{\gamma}_r \gg 1$, the bright state saturates, regardless of the driving direction, and the system returns to its reciprocal behavior.

In order to provide a metric of the isolation capabilities of the quantum diode, we calculate the *diode efficiency* $\mathcal{E} \equiv |t_{\rightarrow}|(|t_{\rightarrow}| - |t_{\leftarrow}|)/(|t_{\rightarrow}| + |t_{\leftarrow}|)$ used in Ref. [16] which, in the ideal case of identical qubits and no decoherence, coincides with the definition of efficiency used in Refs. [15–17]. In spite of relatively low dephasing and non-radiative decay rates ($\gamma_{\phi}, \gamma_{nr} < 0.5\% \bar{\gamma}_r$ for both qubits), the maximum diode efficiency appears to be limited to $\simeq 0.27$, well below its ideal value [18] of $2/3$ (see Fig. 2). This illustrates an experimental challenge in the realization of the quantum diode: since the nonreciprocal behavior relies on populating the quasi-dark state $|+\rangle$, the transition rate relevant for the system dynamics is $\Gamma_+ = \delta^2 \bar{\gamma}_r \ll \bar{\gamma}_r$. In our experiment, the dephasing and dissipation rates, $\gamma_{\phi}, \gamma_{nr}$, are of the same order of magnitude of Γ_+ . This renders the effect of decoherence much more significative compared to single-qubit phenomena, whose dynamics evolve at the much faster rate γ_r .

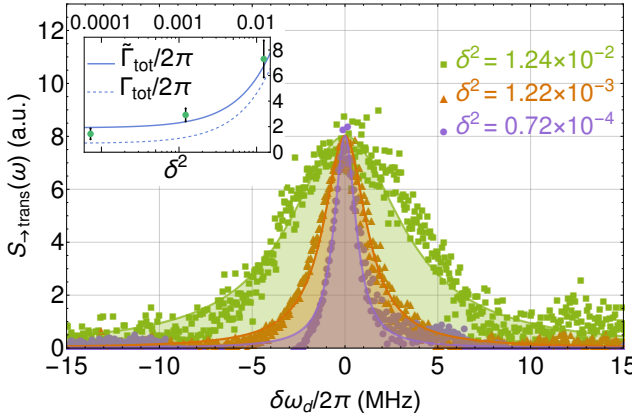


Figure 4. Power spectral densities of the inelastically scattered transmitted field. The system is driven in the forward direction for different detuning regimes ($\delta^2 \simeq 0.01, 0.001, 0.0001$). In every case, the spectra were taken at the optimum atomic detunings and driving powers that maximize the diode efficiency \mathcal{E} . The solid lines are fits to Lorentzians of width 1.43 MHz, 2.92 MHz and 7.30 MHz, in increasing order of δ^2 . As predicted by theory, the linewidth $\Gamma_{\text{FWHM}} \equiv 2(3\delta^2\bar{\gamma}_r + 2\gamma_\phi + \gamma_{nr})$ of the scattered field increases linearly with δ^2 (see inset). However, in the experiment the width of the inelastically scattered radiation is broader than expected: $\tilde{\Gamma}_{\text{tot}} = \Gamma_{\text{tot}} + \Gamma_{\text{exc}}$, with $\Gamma_{\text{exc}}/2\pi = 1.22$ MHz. The elastic part of the scattered radiation at $\delta\omega_d = 0$ MHz has been omitted and the peaks are scaled for clarity.

Further insights into the role of the quasi-dark state can be obtained by measuring the full spectrum of the elastically and inelastically scattered radiation. Notably, the measurement of the power spectral densities, in addition to a δ -like peak due to elastically (Rayleigh) scattered radiation (Fig. 3), features an additional broader peak, which we identify with radiation inelastically scattered off the quasi-dark $|+\rangle$ state. The measured power spectrum agrees with our expectation of the total scattered power being a measure of the population of the quasi-dark state: as clearly seen from the measurement (Fig. 3), the scattered power is much greater when the system is driven in the forward direction.

Being able to control δ , we can tune the linewidth of the dark state emission, $\Gamma_+ = \delta^2\bar{\gamma}_r$. Fig. 4 shows the power spectral densities of scattered radiation for three values of δ (here the elastic part has been omitted for clarity). As expected, the linewidth of the fluorescence spectra increases linearly with δ^2 , following the increase

in the decay rate of the dark state.

Our theoretical estimates predict that the width of the emission peak results from a combination of the dark state linewidth Γ_+ and broadening due to non-radiative and dephasing contributions. In the optimal diode conditions, the linewidth of the transmitted field when driving the system in the forward direction can be found analytically as $\Gamma_{\text{FWHM}} = 2(3\Gamma_+ + 2\gamma_\phi + \gamma_{nr})$ (see Supplementary Material). In the experiment, the width of the inelastically scattered radiation is wider than predicted by 1.22 MHz. This indicates an additional source of noise (presumably of technical origin) which could be mixed with the detected signal and results in an additional broadening of the scattered field.

By incorporating quantum-limited Josephson parametric amplifiers into our detection lines [23], we can measure time-domain single-shot data of the scattered fields and calculate its statistics. Our results show that the in-phase noise is higher when driving the system in the forward direction than in the reverse direction (see Supplementary Material). This is consistent with the statistics produced by replacing the system with a simple stochastic mirror, as theoretically predicted in Ref. [18].

In conclusion, we experimentally realized a passive quantum nonreciprocal device comprised of a minimal number of constituents. Clearly, at least two localized quantum emitters are required to break structural symmetry in 1D space, while a two-level atom is the simplest system presenting a nonlinear quantum behavior. The nonreciprocity relies on the interplay of the exchange interaction and the collective decay of quantum emitters leading to population trapping into an entangled quasi-dark state for a preferred driving direction. While not yet sufficient for practical applications, our results open a path for the realization of more efficient nonreciprocal devices with multiple coherent qubits. The demonstrated mechanism of population trapping is also valuable for the development of protocols of remote entanglement stabilization.

ACKNOWLEDGMENTS

This work was supported by the Australian Research Council under the Discovery and Centre of Excellence funding schemes (project numbers DP150101033, DE160100356, and CE110001013). M.W. acknowledges support from the European Research Council (ERC) under the Grant Agreement 648011.

[1] David M. Pozar, *Microwave Engineering* (Wiley, 1998).
[2] Giovanni Viola and David P. DiVincenzo, “Hall effect gyrators and circulators,” *Phys. Rev. X* **4**, 021019 (2014).
[3] A. C. Mahoney, J. I. Colless, S. J. Pauka, J. M. Hornibrook, J. D. Watson, G. C. Gardner, M. J. Manfra, A. C. Doherty, and D. J. Reilly, “On-chip microwave quantum hall circulator,” *Phys. Rev. X* **7**, 011007 (2017).
[4] Clemens Müller, Shengwei Guan, Nicolas Vogt, Jared H Cole, and Thomas M Stace, “Passive On-Chip Superconducting Circulator Using a Ring of Tunnel Junctions,” *Physical Review Letters* **120**, 213602 (2018).
[5] Nicholas A. Estep, Dimitrios L. Sounas, Jason Soric, and

Andrea Alù, "Magnetic-free non-reciprocity and isolation based on parametrically modulated coupled-resonator loops," *Nature Physics* **10**, 923 (2014).

[6] Joseph Kerckhoff, Kevin Lalumière, Benjamin J. Chapman, Alexandre Blais, and K. W. Lehnert, "On-chip superconducting microwave circulator from synthetic rotation," *Phys. Rev. Applied* **4**, 034002 (2015).

[7] S. Barzanjeh, M. Wulf, M. Peruzzo, M. Kalaee, P. B. Dieterle, O. Painter, and J. M. Fink, "Mechanical on-chip microwave circulator," *Nature Communications* **8**, 953 (2017).

[8] N. R. Bernier, L. D. Tóth, A. Koottandavida, M. A. Ioannou, D. Malz, A. Nunnenkamp, A. K. Feofanov, and T. J. Kippenberg, "Nonreciprocal reconfigurable microwave optomechanical circuit," *Nature Communications* **8**, 604 (2017).

[9] Kejie Fang, Jie Luo, Anja Metelmann, Matthew H. Matherly, Florian Marquardt, Aashish A. Clerk, and Oskar Painter, "Generalized non-reciprocity in an optomechanical circuit via synthetic magnetism and reservoir engineering," *Nature Physics* **13**, 465 (2017).

[10] Benjamin J. Chapman, Eric I. Rosenthal, Joseph Kerckhoff, Bradley A. Moores, Leila R. Vale, J. A. B. Mates, Gene C. Hilton, Kevin Lalumière, Alexandre Blais, and K. W. Lehnert, "Widely tunable on-chip microwave circulator for superconducting quantum circuits," *Phys. Rev. X* **7**, 041043 (2017).

[11] Li Fan, Jian Wang, Leo T. Varghese, Hao Shen, Ben Niu, Yi Xuan, Andrew M. Weiner, and Minghao Qi, "An all-silicon passive optical diode," *Science* **335**, 447–450 (2012).

[12] Yu Yi, Chen Yaohui, Hu Hao, Xue Weiqi, Yvind Kresten, and Mork Jesper, "Nonreciprocal transmission in a nonlinear photonic crystal fano structure with broken symmetry," *Laser & Photonics Reviews, Laser & Photonics Reviews* **9**, 241–247 (2015).

[13] Dimitrios L. Sounas, Jason Soric, and Andrea Alù, "Broadband passive isolators based on coupled nonlinear resonances," *Nature Electronics* **1**, 113–119 (2018).

[14] Bo Peng, ahin Kaya zdemir, Fuchuan Lei, Faraz Monifi, Mariagiovanna Gianfreda, Gui Lu Long, Shanhai Fan, Franco Nori, Carl M. Bender, and Lan Yang, "Parity-time-symmetric whispering-gallery microcavities," *Nature Physics* **10**, 394 (2014).

[15] F. Fratini, E. Mascarenhas, L. Safari, J. Ph Poizat, D. Valente, A. Auffèves, D. Gerace, and M. F. Santos, "Fabry-perot interferometer with quantum mirrors: Non-linear light transport and rectification," *Physical Review Letters* **113**, 1–5 (2014), arXiv:1410.5972.

[16] Jibo Dai, Alexandre Roulet, Huy Nguyen Le, and Valerio Scarani, "Rectification of light in the quantum regime," *Physical Review A - Atomic, Molecular, and Optical Physics* **92**, 1–7 (2015), arXiv:1510.04494.

[17] F. Fratini and R. Ghobadi, "Full quantum treatment of a light diode," *Physical Review A - Atomic, Molecular, and Optical Physics* **93**, 1–5 (2016).

[18] Clemens Müller, Joshua Combes, Andrés Rosario Hamann, Arkady Fedorov, and Thomas M. Stace, "Nonreciprocal atomic scattering: A saturable, quantum Yagi-Uda antenna," *Physical Review A* **96**, 1–10 (2017), arXiv:1708.03450.

[19] Maximilian Zanner, Lukas Gruenhaupt, Silvia Diewald, Andrés Rosario Hamann, Arkady Fedorov, Alexey V. Ustinov, and Martin Weides, "Tunable superconducting qubit in a 3D waveguide," to be submitted.

[20] O. Astafiev, A. M. Zagoskin, A. A. Abdumalikov, Yu. A. Pashkin, T. Yamamoto, K. Inomata, Y. Nakamura, and J. S. Tsai, "Resonance fluorescence of a single artificial atom," *Science* **327**, 840–843 (2010), arXiv:1002.4944.

[21] Kevin Lalumière, Barry C. Sanders, A. F. van Loo, A. Fedorov, A. Wallraff, and A. Blais, "Input-output theory for waveguide qed with an ensemble of inhomogeneous atoms," *Phys. Rev. A* **88**, 043806 (2013).

[22] E. S. Redchenko and V. I. Yudson, "Decay of metastable excited states of two qubits in a waveguide," *Phys. Rev. A* **90**, 063829 (2014).

[23] C. Eichler, Y. Salathe, J. Mlynek, S. Schmidt, and A. Wallraff, "Quantum-limited amplification and entanglement in coupled nonlinear resonators," *Phys. Rev. Lett.* **110** 0502 (2014).

[24] Joshua Combes, Joseph Kerckhoff, and Mohan Sarovar, "The SLH framework for modeling quantum input-output networks," *Advances in Physics: X* **2**, 784–888 (2017).

Appendix A: Measurement setup

The nonreciprocal device, consisting of two superconducting qubits embedded in a 1D waveguide, is mounted on the 20 mK stage of a dilution refrigerator (purple box in Fig. 5). Two superconducting coils mounted around the waveguide serve to control the Josephson inductance of each of the qubits, which in turn determine their transition frequencies f_{qe} .

The device can be driven from any of the two input ports α, β , which are interfaced with the waveguide through the coupled ports of two directional couplers. The reflected and transmitted signals are then collected via the through port of the directional couplers, which allows us to detect them simultaneously. The two output signals are then parametrically amplified via two Josephson parametric dimers (JPD) [23] (orange boxes in Fig. 5) and further amplified via two high-electron-mobility transistor (HEMT) amplifiers.

Appendix B: Single qubit SLH description

For a single atom in a waveguide, coupled symmetrically to both propagation directions, and driven with a coherent field from both sides, we can write, in analogy

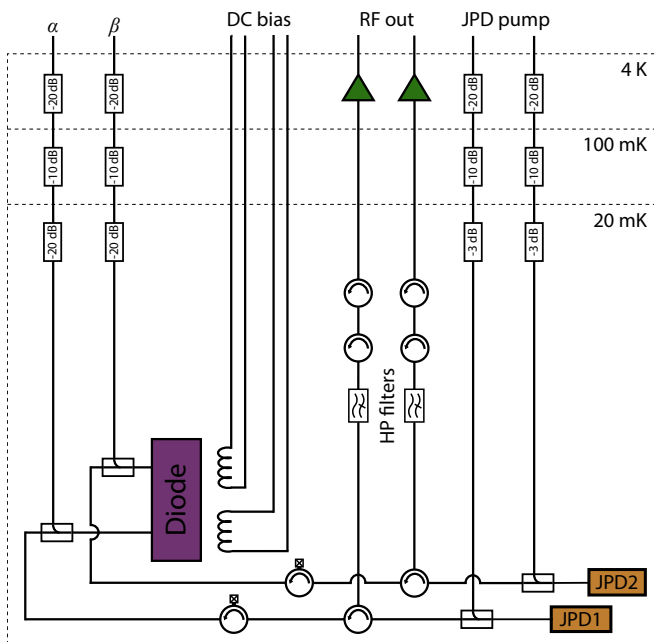


Figure 5. Cryogenic setup. Two qubits embedded in a 1D waveguide (purple box), which can be driven from either of the input lines α, β . After amplification at the Josephson parametric dimers (orange boxes) and high-electron-mobility transistors (green triangles), the transmitted and reflected fields can be simultaneously detected at RF out.

to Ref. [18],

$$H_{\text{tot}} = -\frac{1}{2}\delta\omega\sigma_z + \frac{1}{2i}\sqrt{\frac{\gamma_r}{2}}((\alpha + \beta)\sigma_+ - \text{h.c.}), \quad (\text{B1})$$

$$a_{\text{out}} = \sqrt{\frac{\gamma_r}{2}}\sigma_- + \alpha, \quad b_{\text{out}} = \sqrt{\frac{\gamma_r}{2}}\sigma_- + \beta, \quad (\text{B2})$$

where γ_r is the total radiative decay rate into the waveguide modes, α is the strength of the coherent drive from the left, and β is the driving field amplitude from the right. Here, Eq. (B1) is written in a frame rotating at the drive frequency ω_d , and $\delta\omega = \omega_q - \omega_d$ is the detuning between the atomic transition frequency ω_q and the drive. The master equation, including non-radiative decay and dephasing on the atom, is then

$$\dot{\rho} = -i[H_{\text{tot}}, \rho] + \mathcal{D}[a_{\text{out}}]\rho + \mathcal{D}[b_{\text{out}}]\rho + \gamma_{nr}\mathcal{D}[\sigma_-]\rho + \frac{1}{2}\gamma_\phi\mathcal{D}[\sigma_z]\rho, \quad (\text{B3})$$

with the non-radiative decay rate γ_{nr} and the dephasing rate γ_ϕ .

To calculate the transmittance, we first find the steady-state of the master equation, $\dot{\rho} = 0$. The transmission amplitude when driving from the left is then

$$t = \text{Tr}\{a_{\text{out}}\bar{\rho}\} / \alpha = 1 - \frac{\gamma_r}{2\gamma_2} \frac{1 - i\delta\omega/\gamma_2}{1 + (\delta\omega/\gamma_2)^2 + 2|\alpha|^2\gamma_r/\gamma_1\gamma_2}, \quad (\text{B4})$$

where we defined the total atomic decay rate $\gamma_1 = \gamma_r + \gamma_{nr}$ and dephasing rate $\gamma_2 = \frac{1}{2}\gamma_1 + \gamma_\phi$, and $|\alpha|^2$ is the power of the incoming drive.

Appendix C: Single qubit spectroscopy

We characterize the radiative γ_r , non-radiative γ_{nr} , and dephasing γ_ϕ rates of each individual qubit by performing spectroscopic measurements. In order to achieve this, we detune one of the qubits below the cutoff of the waveguide and set the target qubit to frequency ω_q . We then sweep a low power microwave tone ω_d around ω_q and detect the transmitted electric field E_t . Next, we calculate the transmission amplitude $t = E_t/E_i$, where E_i is the amplitude of the incident electric field. The transmittance is then least-squares fitted to Eq. (B4) to extract all relevant parameters for each qubit individually. We repeat this procedure for a range of target frequencies for each qubit in order to characterize their operational points. The radiative decay rates γ_r are found to vary between $2\pi \times 60$ MHz and $2\pi \times 85$ MHz for qubit frequencies between 8.5 GHz and 9.5 GHz, whereas $\gamma_\phi, \gamma_{nr} < 0.5\%\gamma_r$ throughout this range. See Table I for some particular values.

	8.6 GHz	8.8 GHz
$\gamma_{r,1}/2\pi$ (MHz)	71.3039	62.4261
$\gamma_{r,2}/2\pi$ (MHz)	72.4299	73.1158
$\gamma_\phi/2\pi$ (kHz)	211.4	74.7
$\gamma_{nr}/2\pi$ (kHz)	191.1	64.0

Table I. Least-squares fit results for qubits 1 and 2 tuned to 8.6 GHz and 8.8 GHz. We use the methods outlined in App. C to fit $\gamma_{r,i}$ and $\gamma_{nr} + 2\gamma_\phi$. We assume equal dephasing and non-radiative decay rates for both qubits. We then use the two-qubit transmission amplitude expressions found in App. D to get individual values for γ_{nr} and γ_ϕ when the device is configured in the diode regime.

Appendix D: Two-qubit master equation

Following Ref. [18], we write the master equation for the two-qubit density matrix

$$\dot{\rho} = \mathcal{L}\rho \equiv -i[H_T, \rho] + \mathcal{D}[a_{\text{out}}]\rho + \mathcal{D}[b_{\text{out}}]\rho + \gamma_{nr}(\mathcal{D}[\sigma_-^{(1)}]\rho + \mathcal{D}[\sigma_-^{(2)}]\rho) + \gamma_\phi(\mathcal{D}[\sigma_z^{(1)}]\rho + \mathcal{D}[\sigma_z^{(2)}]\rho), \quad (\text{D1})$$

where $\mathcal{D}[X]\rho = X\rho X^\dagger - \frac{1}{2}(X^\dagger X\rho + \rho X^\dagger X)$, and

$$\begin{aligned} H_T &= H_1 + H_2 - i(\alpha L_1^\dagger - \alpha^* L_1)/2 - i(\beta L_2^\dagger - \beta^* L_2)/2 \\ &\quad - i(e^{i\phi} L_2^\dagger (L_1 + \alpha) - e^{-i\phi} (L_1^\dagger + \alpha^*) L_2)/2 \\ &\quad - i(e^{i\phi} L_1^\dagger (L_2 + \beta) - e^{-i\phi} (L_2^\dagger + \beta^*) L_1)/2, \\ a_{\text{out}} &= (\alpha + L_1)e^{i\phi} + L_2, \\ b_{\text{out}} &= (\beta + L_2)e^{i\phi} + L_1. \end{aligned}$$

Here α, β are the amplitudes of the right- and left-moving fields, respectively, and the operators a_{out} and b_{out} represent the right- and left-moving output fields. The input field is at frequency ω_d , ϕ is the phase shift acquired by the drive when traveling between the atoms, and L_i, H_i form part of the SLH triplet [24] described by

$$H_k = -\omega_k \sigma_z^{(k)}/2, \quad L_k = \sqrt{\gamma_{r,k}/2} \sigma_-^{(k)},$$

where $k = 1, 2$ indexes the atoms, ω_k is the eigenfrequency of atom k in the frame rotating at ω_d , and $\gamma_{r,k}$ is its radiative decay rate. We defined the atomic lowering operator as $\sigma_- = |g\rangle\langle e|$.

The right-moving steady-state output field is then found as $\langle a_{\text{out}} \rangle_{SS}^{(\alpha, \beta)} = \text{Tr} \{ a_{\text{out}} \rho_{SS}^{(\alpha, \beta)} \}$, where $\rho_{SS}^{(\alpha, \beta)}$ is the steady state solution of Eq. D1, $\dot{\rho}_{SS}^{(\alpha, \beta)} = 0$, with input amplitudes α, β . Finally, we calculate the forward-driven transmission amplitude as $t_f = \langle a_{\text{out}} \rangle_{SS}^{(\alpha, 0)}/\alpha$. Similarly, the reverse-driven transmission amplitude equates to $t_r = \langle b_{\text{out}} \rangle_{SS}^{(0, \beta)}/\beta$.

Appendix E: Bright and dark states decay rates for $\gamma_{r,1} \neq \gamma_{r,2}$

Following the notation of Ref. [18], we write the dissipative parts of the SLH dissipators as

$$\begin{aligned} \bar{L}_1 &= \frac{1}{2} \{ \sqrt{\gamma_{r,1}} (\sigma_-^D - \sigma_-^B) + \sqrt{\gamma_{r,2}} e^{i\phi} (\sigma_-^D + \sigma_-^B) \}, \\ \bar{L}_2 &= \frac{1}{2} \{ \sqrt{\gamma_{r,2}} (\sigma_-^D + \sigma_-^B) + \sqrt{\gamma_{r,1}} e^{i\phi} (\sigma_-^D - \sigma_-^B) \}, \end{aligned}$$

where we assumed the general case of $\gamma_{r,1} \neq \gamma_{r,2}$, and we used the dark and bright state annihilation operators

$$\begin{aligned} \sigma_-^D &= \frac{1}{\sqrt{2}} (\sigma_-^{(2)} + \sigma_-^{(1)}), \\ \sigma_-^B &= \frac{1}{\sqrt{2}} (\sigma_-^{(2)} - \sigma_-^{(1)}). \end{aligned}$$

In the experimentally relevant limit where $\phi = \pi - \delta$, $\delta \ll \gamma_{r,k}$, and $\gamma_{r,1} \approx \gamma_{r,2}$, we can rewrite the the sum of dissipators in the master equation as

$$\mathcal{D}[\bar{L}_1]\rho + \mathcal{D}[\bar{L}_2]\rho \simeq \gamma_D \mathcal{D}[\sigma_-^D]\rho + \gamma_B \mathcal{D}[\sigma_-^B]\rho, \quad (\text{E1})$$

with $\gamma_D = \delta^2 \bar{\gamma}_r/2$ and $\gamma_B = 2\bar{\gamma}_r$, and where we defined $\bar{\gamma}_r \equiv \sqrt{\gamma_{r,1}\gamma_{r,2}}$.

Appendix F: Linewidth of the transmitted field

The linewidth of the dark state emission is given by the lifetime of the dark state population p_D , i.e., the rate at which it decays towards its equilibrium state. In the diode regime, the dark state is inverted, in that $p_D > 1/2$. Without nonradiative decay or additional dephasing, from Ref. [18] we find the decay rate of the dark state into the ground-state in the diode regime as $\gamma_D = \delta^2 \bar{\gamma}_r/2$. In the same regime, the excitation rate of exciting the ground state into the dark state is $\gamma_{\uparrow D} = 2\gamma_D$, leading to the ideal steady-state dark state population of $p_D = \gamma_{\uparrow D}/(\gamma_{\uparrow D} + \gamma_D) = 2/3$.

In the non-ideal case, assuming symmetric nonradiative and dephasing as in Eq. (D1), and focusing on their contributions to the dark state decay rate, one finds

$$\gamma_{nr} (\mathcal{D}[\sigma_-^{(1)}]\rho + \mathcal{D}[\sigma_-^{(2)}]\rho) = \gamma_{nr} (\mathcal{D}[\sigma_-^D]\rho + \mathcal{D}[\sigma_-^B]\rho), \quad (\text{F1})$$

$$\gamma_\phi (\mathcal{D}[\sigma_z^{(1)}]\rho + \mathcal{D}[\sigma_z^{(2)}]\rho) = \frac{\gamma_\phi}{2} \mathcal{D}[\sigma_z^1 + \sigma_z^2]\rho + 2\gamma_\phi \mathcal{D}[\sigma_-^D]\rho, \quad (\text{F2})$$

leading to the total decay rate of the dark state $\gamma'_D = \gamma_D + \gamma_{nr} + 2\gamma_\phi$. The dark state lifetime is then $\Gamma_D = \gamma'_D + \gamma_{\uparrow D} = 3\gamma_D + \gamma_{nr} + 2\gamma_\phi$ and the experimentally measured total linewidth of the emitted radiation is given by $\Gamma_{\text{FWHM}} = 2\Gamma_D$.

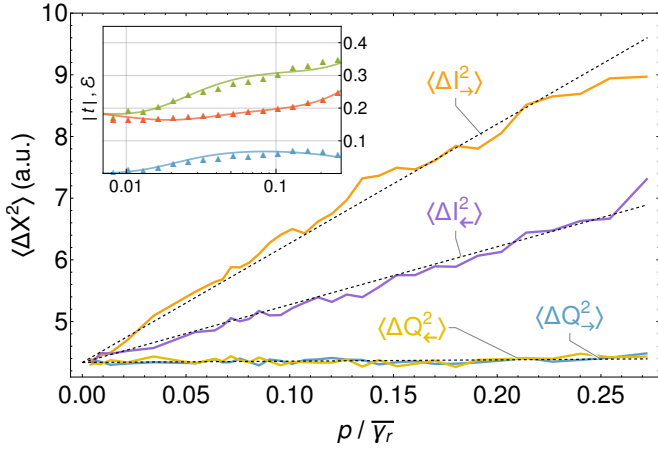


Figure 6. Variance of the single-shot detected output fields with increasing power. The device was prepared at the optimum diode configuration for $\delta^2 \simeq 0.01$. At each power, 2^{18} single shots of the forward and reverse driving heterodyne IQ signal were detected at a 100 MHz rate. The statistics of the collected data features a linear dependence with power in the in-phase noise $\langle \Delta I_{\rightarrow}^2 \rangle$, consistent with a constant population of the quasi-dark state. The quadrature noise remains at a constant value, regardless of the driving direction, $\langle \Delta Q_{\rightarrow}^2 \rangle = \langle \Delta Q_{\leftarrow}^2 \rangle = \sigma_w^2 = \sigma_{\text{qn}}^2 + \sigma_{\text{tech}}^2$, where σ_{tech}^2 and σ_{qn}^2 are the technical and quantum noise contributions to the signal, respectively. Due to a limitation in the frequency tuning range of the Josephson parametric amplifiers, the measurement was performed in a separate cooldown for a larger distance between qubits $d = 44.95$ mm and at a lower driving frequency $\omega_d/2\pi \simeq 7.398$ GHz. At this regime, the diode efficiency \mathcal{E} was found to be limited to 0.07. Inset: Experimental data (points) and theoretical fits (solid lines) for the forward (green) and reverse (red) transmission amplitudes. The diode efficiency \mathcal{E} is plotted in blue.

Appendix G: Output field statistics in the diode configuration

When driving the diode in the forward direction and powers $p/\bar{\gamma}_r \ll 1$, the system is confined to the $\{|G\rangle, |D\rangle\}$ manifold (up to order δ^2). The two-atom system can be found in the ground, reflecting state with probability $(1 - P_D)$ or in the quasi-dark, transparent state with probability P_D . As demonstrated in Ref. [18], the statistics

of the scattered fields in the diode regime can be replicated by a *flapping mirror* model, i.e., by a system composed of a stochastic mirror that can flip into the path of the signal (reflecting state, $X = 0$) with probability $(1 - P_D)$, or out of the path (transmitting state, $X = 1$) with probability P_D . In this scenario, the transmitted in-phase heterodyne signal I can be modeled as $I(t) = S(t) + w(t)$, where $S(t) = \alpha X(t)$ is the transmitted signal, which depends on the driving amplitude α and the state of the mirror X , and $w(t)$ encompasses both quantum and technical noise contributions. Assuming uncorrelated white noise, such that $\bar{w} = 0$, the variance of the in-phase signal is given by

$$\begin{aligned} \langle \Delta I^2 \rangle &= \langle (S(t) + w(t) - \bar{S})^2 \rangle \\ &= \langle (S(t) - \bar{S})^2 \rangle + \langle w(t)^2 \rangle \\ &= \sigma_S^2 + \sigma_w^2. \end{aligned}$$

Since $S(t) = \alpha X(t)$, $\sigma_S^2 = |\alpha|^2 \sigma_X^2 = |\alpha|^2 P_D (1 - P_D)$, which gives

$$\langle \Delta I^2 \rangle = |\alpha|^2 P_D (1 - P_D) + \sigma_w^2.$$

On the other hand, the quadrature signal remains unchanged regardless of the state of the mirror $Q(t) = w(t)$, and hence $\langle \Delta Q^2 \rangle = \sigma_w^2$. In both the forward- and reverse-driving configurations, the noise in the reflected and transmitted signals is the same since $R(t) = 1 - S(t)$.

We incorporate quantum-limited Josephson parametric amplifiers into our detection lines in order to measure time-domain single-shot data of the scattered fields and compare our results to the flapping mirror model (see Fig. 6). When forward-driving the system with powers $p/\bar{\gamma}_r \ll 1$, the quasi-dark state population $P_{D,\rightarrow}$ reaches a constant non-zero value (up to order δ^2), and hence we observe that the in-phase noise scales linearly with power: $\langle \Delta I_{\rightarrow}^2 \rangle = C_1 + C_2 p$. As expected, the quadrature noise remains at its constant value for both driving directions $\langle \Delta Q_{\rightarrow}^2 \rangle = \langle \Delta Q_{\leftarrow}^2 \rangle = \sigma_w^2 = \sigma_{\text{qn}}^2 + \sigma_{\text{tech}}^2$, where σ_{tech}^2 and σ_{qn}^2 are the technical and quantum noise contributions to the signal, respectively. The in-phase noise for the reverse driving scattered field $\langle \Delta I_{\leftarrow}^2 \rangle$ also increases linearly with power, although at a different rate, consistent with a smaller population $P_{D,\leftarrow} < P_{D,\rightarrow}$ of the quasi-dark state and with our simulations.